ROTATIONAL TESTBED FOR COULOMB INDUCED SPACECRAFT ATTITUDE CONTROL

Daan Stevenson and Hanspeter Schaub

5th International Conference on Spacecraft Formation Flying Missions and Technologies

ROTATIONAL TESTBED FOR COULOMB INDUCED SPACECRAFT ATTITUDE CONTROL

Daan Stevenson[1] **and Hanspeter Schaub**[2]
[1,2]*University of Colorado, 431 UCB, Boulder, CO 80309, USA*
[1]*daan.stevenson@colorado.edu*
[2]*hanspeter.schaub@colorado.edu*

Abstract: *A terrestrial testbed designed to investigate the torques between non-symmetric charged bodies is introduced. In practice these torques may be used by spacecraft for touchless remote attitude control. The experimental system consists of a charged cylinder that rotates about its minor axis on a low friction bearing, while the electric potential on a nearby sphere is actively controlled to increase or decrease the rotation rate of the cylinder. A numerical simulation of the system that uses a previously developed reduced order electrostatic model is found to match the experimental data extremely well. Time dependent charge drain and disturbance torques on the cylinder are characterized so that they may be accurately modeled in the simulation. At low speeds, the achievable Coulomb torques are several times higher than the atmospheric drag and bearing friction. An active charge control de-spin maneuver arrests the cylinder motion in about 1/3 of the time it takes the cylinder to come to rest due to the friction in the system alone. Several hardware components and methods are identified for improvement in future iterations of the testbed, but the current result constitutes a successful verification of the Coulomb spacecraft de-spin concept.*

1 Introduction

Incidental electric charging is inherent in any spacecraft mission due to the interaction with the plasma environment both in Earth orbit and interplanetary space. NASA's ATS-5 and ATS-6 missions in 1969 and 1974 tested measurement capability of the spacecraft electrostatic potential and observed ambient charging up to -10kV in solar eclipse. [1] Active voltage control with ion or electron emission devices, as tested in space on the 1979 SCATHA mission, [2] is possible up to $\pm$10s of kV within milliseconds and at sub-milliWatt power levels. [3] Generally, charge control devices are installed on satellites to mitigate natural charging and prevent electric anomalies, but a recent research effort has identified the feasibility of using Coulomb charge control to affect the relative motion of satellites flying in close proximity. [3, 4] The use of electrostatic actuation is attractive for formation flying over conventional thrusters because non-renewable fuel reserves are not depleted and plume impingement issues are avoided. Moreover, if a spacecraft can impart relative potentials on itself and an inactive craft using a focused charged beam, touchless electrostatic maneuvers may be achieved within non-cooperative formations. [5] One limitation of this technology is the effect of plasma in the (Low Earth Orbit) LEO regime, which causes considerable Debye shielding of the electrostatic fields. Spacecraft formations at the sparser Geosynchronous (GEO) space environment, however, can exert milliNewton level electrostatic forces at separation distances of tens of meters using 10s of kiloVolts of potential. [3]
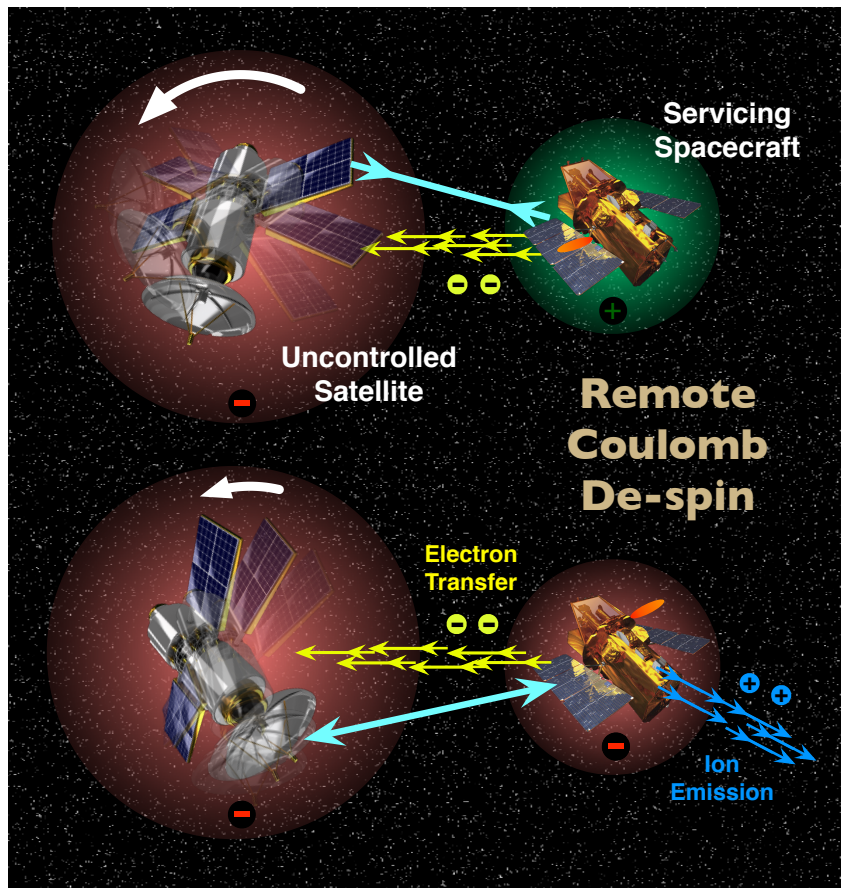
Figure 1. Depiction of the remote Coulomb de-spin concept

Investigation of the charged Coulomb interaction between non-spherical bodies suggests that prolate bodies can experience torques and off-axis forces. [6] If these torques can be harnessed to remotely decrease the rotation of non-cooperative bodies with large moments of inertia and angular momenta, the tradespace of candidate spacecraft for rendezvous and docking operations can be greatly increased. Pose algorithms and attitude matching maneuvers for rendezvous are generally limited to rotation rates below 1 deg/s. [7] However, implementation of the remote Coulomb de-spin concept depicted in Figure 1 could reduce ambient rotation rates prior to docking operations. This technology is applicable to various mission scenarios intended to ameliorate the expanding orbital debris situation at GEO. [8] First, while an electrostatic tug can be used to increase the semi-major axis of a GEO debris object by 300 km in two months, [9, 10] a docked Hohmann transfer would accomplish this in just over 12 hours. By remotely reducing the rotation rate prior to rendezvous, collision risks and guidance and control challenges are greatly reduced during docking operations. An alternative to repositioning derelict satellites into a graveyard orbit is to service them by replenishing fuel reserves or repairing failed components. Such missions, as investigated by NASA's Satellite Servicing Capability Office and DARPA's Phoenix program, preclude the unnecessary insertion of replacement satellites.

In order to accurately predict the relative motion dynamics of Coulomb spacecraft formations and develop appropriate charge control strategies, the electrostatic interactions must be modeled with high fidelity. Figure 2 compares the accuracy and computational cost of various electrostatic models. During previous research efforts, charged

spacecraft are modeled by point charges [11] or by conducting spheres. [12] Because they lack the ability to resolve the charge distribution in non-symmetric bodies, these methods are incapable of predicting electrostatic torques and off-axis forces. The Finite Element Analysis (FEA) approach at the other end of the spectrum yields highly accurate numerical solutions, but lacks the computational speed necessary for 6 Degree of Freedom (6DOF) charged relative motion simulations. The recently developed Multi-Sphere Method (MSM) uses a set of conductive spheres throughout the geometry of a spacecraft to capture the 3D electrostatic effects, thus achieving the desired balance between computational efficiency and accuracy. A reduced number of spheres can be distributed within the volume of simpler geometries, [13] or a larger number can be used to uniformly populate the surface of more complex shapes. [14] The MSM is utilized to investigate the Lyapunov stability and simulate implementation of the nonlinear control algorithms necessary for the remote de-spin of a rotating cylinder by active Coulomb charging. [15] It is desirable to further verify this concept experimentally, and this paper outlines the terrestrial testbed that has been developed to do so.
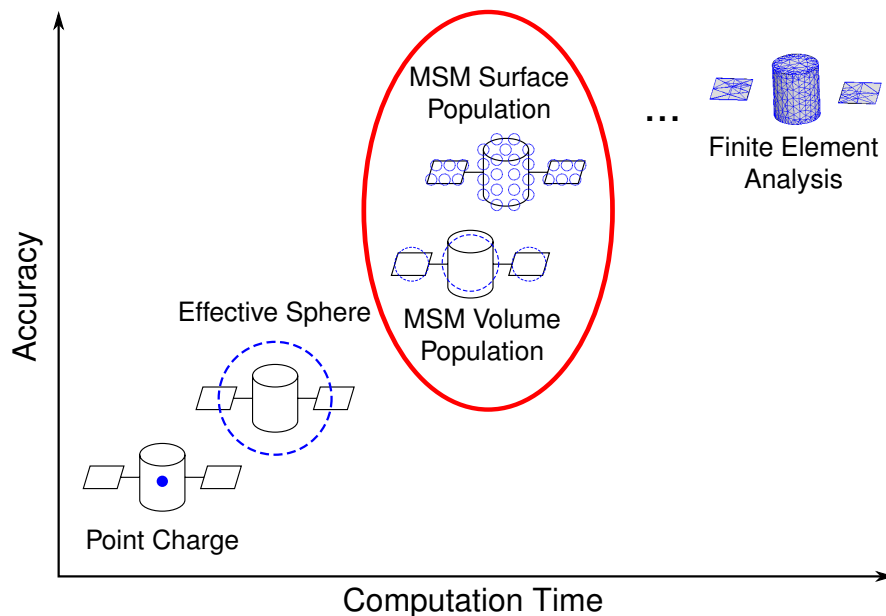

Figure 2. Comparison of various electrostatic models

2   Multi-Sphere Method

The Multi Sphere Model (MSM) framework is presented here as applied to the cylinder-sphere system shown in Figure 3. [15] The cylinder shape is representative of many upper stage rocket bodies such as the Centaur, which may experience a tumbling motion that must be removed if any spacecraft wishes to perform a docking maneuver. While it is possible to capture the induced charge effects that occur at very close proximity scenarios with a larger set of spheres distributed on the surface of the objects, [14] three spheres are sufficient to capture the torques exerted on the cylinder at larger separations distances.

The defining system parameters are the separation distance d, the cylinder orientation angle θ, and the control voltages ϕ_1 and ϕ_2. The spheres in the cylinder are separated
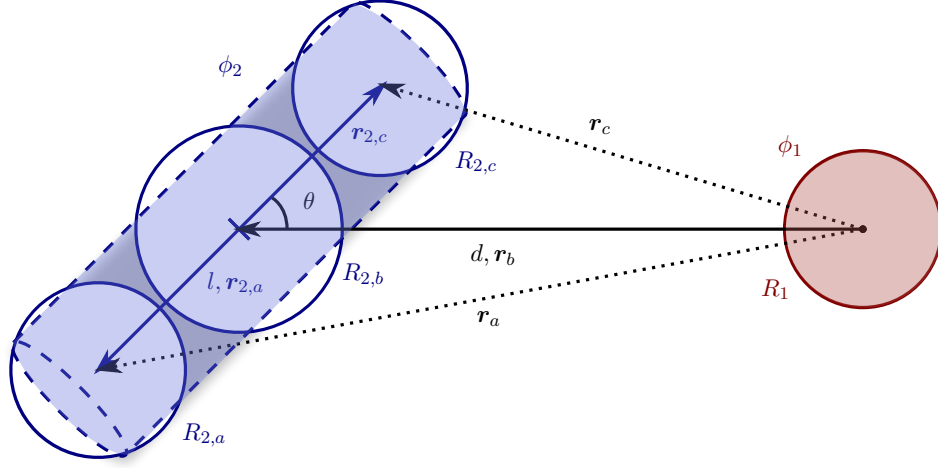
3

Figure 3. 3-sphere MSM for cylinder-sphere configuration

by l while the remaining relative distances are:

$$r_a = \sqrt{l^2 + d^2 + 2ld\cos\theta} \tag{1}$$

$$r_b = d \tag{2}$$

$$r_c = \sqrt{l^2 + d^2 - 2ld\cos\theta} \tag{3}$$

The electrostatic forces are determined by the charges residing on each sphere. These result from the prescribed electric potentials, according to the self and mutual capacitance relationships in Eq. (4), where $k_c = 8.99 \times 10^9$ Nm²/C² is Coulomb's constant: [16, 17, 12]

$$\phi_i = k_c \frac{q_i}{R_i} + \sum_{j=1, j\neq i}^{m} k_c \frac{q_j}{r_{i,j}} \tag{4}$$

These relations can be combined for each sphere to obtain the matrix equation

$$\begin{bmatrix} \phi_1 \\ \phi_2 \\ \phi_2 \\ \phi_2 \end{bmatrix} = k_c \underbrace{\begin{bmatrix} 1/R_1 & 1/r_a & 1/r_b & 1/r_c \\ 1/r_a & 1/R_{2,a} & 1/l & 1/2l \\ 1/r_b & 1/l & 1/R_{2,b} & 1/l \\ 1/r_c & 1/2l & 1/l & 1/R_{2,c} \end{bmatrix}}_{[C_M]^{-1}} \begin{bmatrix} q_1 \\ q_a \\ q_b \\ q_c \end{bmatrix} \tag{5}$$

By inverting $[C_M]^{-1}$, the charge on each sphere is determined at any instance of time. The total electrostatic force and torque about the center of the cylinder are then given by the summations

$$\boldsymbol{F}_2 = k_c q_1 \sum_{i=a}^{c} \frac{q_i}{r_i^3} \boldsymbol{r}_i \tag{6}$$

$$\boldsymbol{M}_2 = k_c q_1 \sum_{i=a}^{c} \frac{q_i}{r_i^3} \boldsymbol{r}_{2,i} \times \boldsymbol{r}_i \tag{7}$$

For this system, Eq. (7) simplifies to

$$M_2 = k_c q_1(d, \theta) ld \sin\theta \left(\frac{q_c(d, \theta)}{r_c^3(d, \theta)} - \frac{q_a(d, \theta)}{r_a^3(d, \theta)} \right) \tag{8}$$

4

Meanwhile, there is a net attractive or repulsive force acting between the two objects in the system. In space, the control craft (the sphere) must create a thrusting force to oppose this Coulomb interaction, thus providing the external influence needed to remove the cylinder's angular momentum from the system. In the terrestrial experiment, the sphere mount and cylinder bearing provide the constraints necessary to oppose these Coulomb forces.

3   Experimental Setup

All hardware components of the terrestrial testbed for electrostatic attitude control are shown in Figure 5. The cylinder, constructed with a conducting surface, has a 15 cm diameter and a 45 cm length. The mass of the rotating components is 182.1 g, with a transverse moment of inertia of 3.30 g·m^2. The 15 cm diameter stationary sphere has a 15 cm surface to surface separation from the cylinder at a parallel orientation with $\theta = 0°$. Table 1 gives the dimensions as outlined in Figure 3, where the MSM parameters are scaled down from the optimized set found in Ref. [13].

Table 1. Parameters for cylinder attitude control system

Parameter	Value	Units	Description
m_{cyl}	182.1	g	Cylinder mass
I_{cyl}	3.30	g·m^2	Cylinder transverse moment of inertia
d	45	cm	Object center-to-center separation
l	17.353	cm	MSM Parameters
R_a, R_c	8.8634	cm	MSM Parameters
R_b	9.7664	cm	MSM Parameters

The three critical components for the rotational Coulomb testbed are low friction rotation, angular position feedback, and high voltage electrostatic control. Several options were considered to achieve frictionless rotation for the cylinder. Ultimately, a full ceramic miniature ball bearing was implemented. Friction disturbance torques are minimal, as characterized in the next section, and the material functions as a successful insulator between the charged cylinder and the base on which the bearing is mounted.
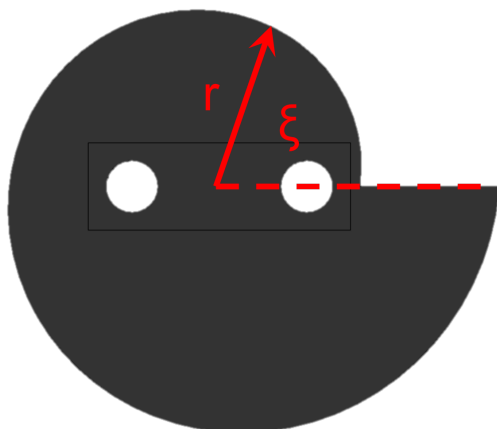

Figure 4. Custom linear - rotational measurement conversion part

To apply the desired Coulomb attitude control algorithms, knowledge of the rotational position of the cylinder is necessary. The USB-input laser distance sensor from the heritage linear Coulomb testbed is currently utilized to make this measurement. It is focused on the varying radius edge of the custom CNC machined plastic part in Figure 4, which rotates along with the cylinder. The radius is equal to $r = 1 + \xi/2\pi$ inches so that an absolute angle can be deduced from the linear measurement. The bottom is recessed in such a way that the inertial axis remains aligned with the axis of rotation on the bearing. The laser is capable of a 50 Hz sampling frequency, but because it
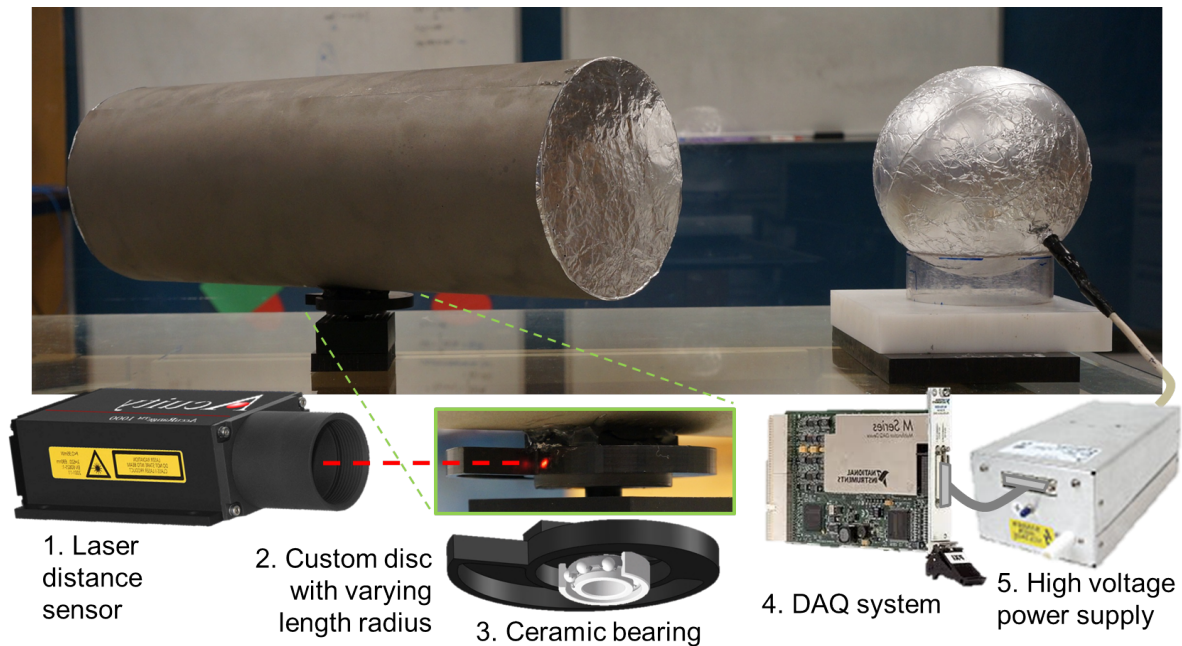
Figure 5. Components of the terrestrial testbed for electrostatic attitude control

is intended for longer range measurement, the output is inherently noisy on the one inch variation surface. A roughly 2 Hz error oscillation with a 1σ standard deviation of 2 deg is identified. When differentiated to determine the speed and acceleration of the rotating cylinder, the noise can lead to severe uncertainties in the results. As such, a 1st order low pass filter is applied at each differentiation step, with a cut-off frequency $\omega_v = 1$ Hz for the angular velocity and $\omega_v = 0.1$ Hz for the angular acceleration. A similar in-situ filter is applied when determining the angular velocity for the Coulomb control algorithms.

For the voltage control of the external sphere and the initial charging of the cylinder, two Spellman CZE 2000 high voltage power supplies are used. They are capable of supplying ± 30 kV at up to 300 μA, which results in power levels well within typical safety limits when proper precaution measures are practiced. One limitation of the power supplies is that they exhibit a slight reduction in output magnitude and a time delay as large as 1 second when switching polarities. [18] For the simulations presented in this paper, the lag is modeled as a constant 0.8 second delay whenever the voltage switches from zero to a non-zero quantity. The power supplies are controlled by a PCI express based 16-Bit multi-channel NI DAQ card. The entire system is monitored and directed by a custom GUI developed with Mac OS-X's native objective C architecture Cocoa. The following list identifies the manufacturer and model numbers for all the hardware mentioned above.

1. Laser distance sensor: *Acuity Laser Measurement AccuRange AR1000*

2. Custom disc with varying length radius - machined in-house

3. Ceramic bearing: *608-2RS 8x22x7 full ceramic sealed bearing*

4. DAQ system: *National Instruments PXI-6259 data acquisition card and (2X) NI SCB-68 shielded breakout boxes*

5. High voltage power supply: *Spellman Voltage Electronics Corporation CZE 2000*

6

3.1 Modeling disturbances

Besides the Coulomb interaction with the sphere, the clearly identifiable disturbances acting on the cylinder as it rotates about its axis are the friction torque from the bearing and the atmospheric drag force acting on the cylinder surface.

The friction torque M_B in a rolling bearing is due to a combination of radial forces and axial forces F_i, the friction coefficient μ_i and the average of the bore and outside diameter of the bearing $\bar{d} = \frac{d_i + d_o}{2}$, as follows:

$$M_B = \mu_r \frac{\bar{d}}{2} F_r + \mu_a \frac{\bar{d}}{2} F_a \tag{9}$$

Since the expected radial force due to the Coulomb interaction with the sphere never exceeds 13.90 mN, whereas the weight of the cylinder and laser disc is equal to a 1.786 N axial force, the radial component can be neglected. If the bearing diameter is incorporated into a new combined bearing friction coefficient γ, the total bearing friction is written

$$M_B = \gamma F_a \tag{10}$$

where γ will be determined empirically.

For high Reynolds number flows, the drag force F_D on a body with surface area A and drag coefficient C_d moving at velocity V through a medium with density ρ is given by

$$F_D = \frac{1}{2} \rho V^2 C_d A \tag{11}$$

Consider a cylinder with length L and diameter D rotating at angular rate ω. A differential slice of width $\mathrm{d}r$ located at a distance r away from the cylinder axis of rotation experiences a drag force

$$\mathrm{d}F_D = \frac{1}{2} \rho (\omega r)^2 C_d (D \mathrm{d}r) \tag{12}$$

The differential torque from each slice is $dM = rdF$ and the total torque from both halves of the cylinder due to atmospheric drag is

$$M_D = \rho \omega^2 C_d D \int_0^{L/2} r^3 \, \mathrm{d}r \tag{13}$$

$$M_D = \frac{\rho \omega^2 C_d D L^4}{64} \tag{14}$$

A typical atmospheric air density $\rho = 1.194$ kg/m³ is used and C_D is found to be 1 for an infinite cylinder at mid-range Reynold numbers. [19] The parasitic drag across the two ends of the cylinder must be considered. Since the ends move at $V = \omega \frac{L}{2}$ relative to the ambient air, this effect can be incorporated in the empirically determined C_d value.

3.2 Empirical Determination of Disturbance Parameters

Both modeled disturbance phenomena contain an unknown coefficient that must be determined empirically. Five sets of data are collected by giving the cylinder an initial rotation and allowing it to de-spin naturally while the electric potential on both the cylinder and the adjacent sphere are held at zero. Figure 6(a) shows the angular rates

of the cylinder for each experimental run and a simulated de-spin using the modeled disturbance torques from Eq. (10) and (14). The corresponding coefficients were tuned until the resultant angular velocity curve fit the experimental data well, resulting in $\gamma = 0.00003$ and $C_d = 1.05$. Figure 6(b) shows the resulting disturbance torques in the simulation, suggesting that the drag force is dominant at angular rates higher than 38 deg/s.
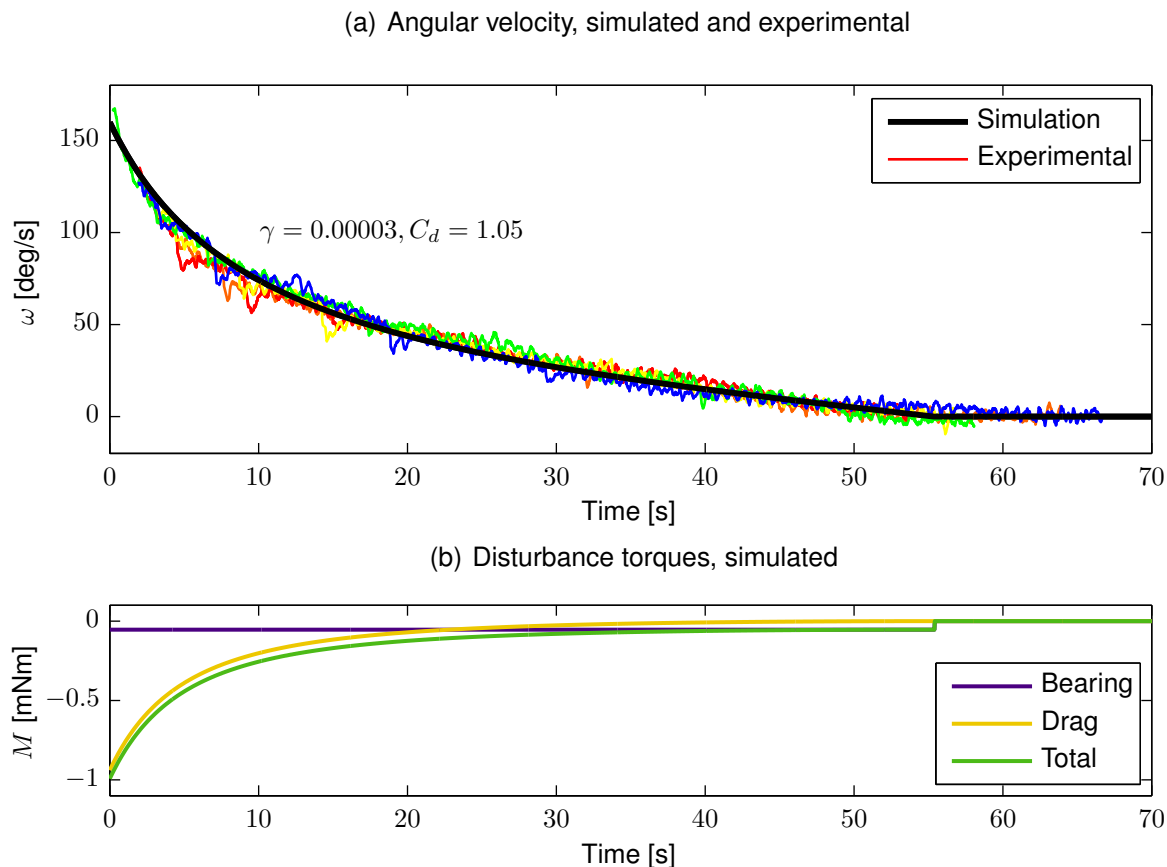
(a) Angular velocity, simulated and experimental

(b) Disturbance torques, simulated

Figure 6. Characterization of disturbance torques

4 Passive charging

Active charging of a spinning cylinder is difficult to implement while minimizing disturbance torques at the bearing about which the cylinder rotates. Therefore, in this iteration of the testbed, passive charging is employed. While the electric potential on the sphere is actively controlled throughout the experiment, the cylinder is brought to a desired voltage initially, after which the charging lead is removed and the cylinder is left with a floating charge. In order to accurately model this scenario, modifications must be made to the MSM to account for a body that carries a specific charge instead of maintaining a prescribed voltage. Moreover, the natural charge drain due to interaction with the atmospheric environment and the insulated bearing module must be characterized.

8

4.1 MSM Modification

Assuming no charge bleeding for now, the scenario presented above entails that the cylinder maintains a total charge

$$q_2 = q_a + q_b + q_c \tag{15}$$

determined by the configuration at which the charge lead is removed. From this point on, ϕ_2 is an unknown dependent on ϕ_1 and the relative position and orientation of the two conductors, but there is also an extra linear equation in Eq. (15). In order to isolate all the unknowns in Eq. (5) into a single column vector, the matrix equation must be modified as follows:

$$\begin{bmatrix} \phi_1/k_c \\ 0 \\ 0 \\ 0 \\ q_2 \end{bmatrix} = \begin{bmatrix} 1/R_1 & 1/r_a & 1/r_b & 1/r_c & 0 \\ 1/r_a & 1/R_{2,a} & 1/l & 1/2l & -1 \\ 1/r_b & 1/l & 1/R_{2,b} & 1/l & -1 \\ 1/r_c & 1/2l & 1/l & 1/R_{2,c} & -1 \\ 0 & 1 & 1 & 1 & 0 \end{bmatrix} \begin{bmatrix} q_1 \\ q_a \\ q_b \\ q_c \\ \phi_2/k_c \end{bmatrix} \tag{16}$$

It is necessary to incorporate the factor k_c with the electric potential terms prior to this modification to ensure that the matrix that must be inverted remains well-conditioned. This approach can be extended for any system where a conductor contains a floating charge rather than being held at a specific voltage.

4.2 Surface Voltmeter Measurements

Measuring the electrostatic potential on a conducting body with a floating charge is not achievable with conventional high voltage measurement equipment. Using the MSM, which is shown to accurately predict the capacitance of a modeled geometry, [14] the capacitance of the 45 cm by 15 cm cylinder is 1.6407×10^{-11} C/V. Even if a contact voltmeter with 1 GΩ impedance is used, the time constant $\tau = RC$ of the measurement circuit is a small fraction of a second, thus preventing accurate measurements. Instead, an Alpha-Lab Inc. Model SVM2 DC Surface Voltmeter

Figure 7. AlphaLab Inc. Surface DC Voltmeter, Model SVM2

as shown in Figure 7 is used to quantify the voltage and charge present on the floating cylinder. The metal disc on the rear of the voltmeter is connected to a high impedance amplifier. When the disc is in the presence of an electric field, charged particles are drawn from the circuit to the surface of the disc, which is measured by the amplifier. The meter is calibrated so that when the disc is held a prescribed distance from a conducting surface, the voltage on the object can be deduced. The measurement range is specified to ± 30 kV, but in reality the meter saturates at roughly -16 kV and only $+6$ kV due to the presence of positive ions.

The SVM2 surface voltmeter was used to measure the remaining voltage on the cylinder for 120 seconds after it was charged to $V = -15$ kV and the charging lead was

removed and controlled to $0\ V$. The orientation of the cylinder was held at both $\theta = 0°$ (parallel) and $\theta = 90°$ (perpendicular) orientations, while the voltage on the nearby sphere was varied between ± 15 kV. The results are plotted in Figure 8(a), from which it is clear that the perpendicular orientation drains charge faster than the parallel orientation, while the opposite sphere polarity case drains voltage faster than the same polarity one. For each scenario, measurements were taken along the minor axis of the cylinder as well as the major axis, but the variation was minor and no trends were discernible between the two, as expected because the conducting cylinder represents an equipotential surface. Figure 8(b) shows an extended time measurement of the median case. As the trend suggests an initial exponential drop followed by a linear decline in voltage, the function

$$V(t) = V_0[0.87 - 0.00041t + 0.127e^{-0.017t}] \tag{17}$$

is fit to the curve, with $R^2 = 0.9996$. A charge drain with these parameters is implemented in the active charge control simulations designed to match the experimental results.
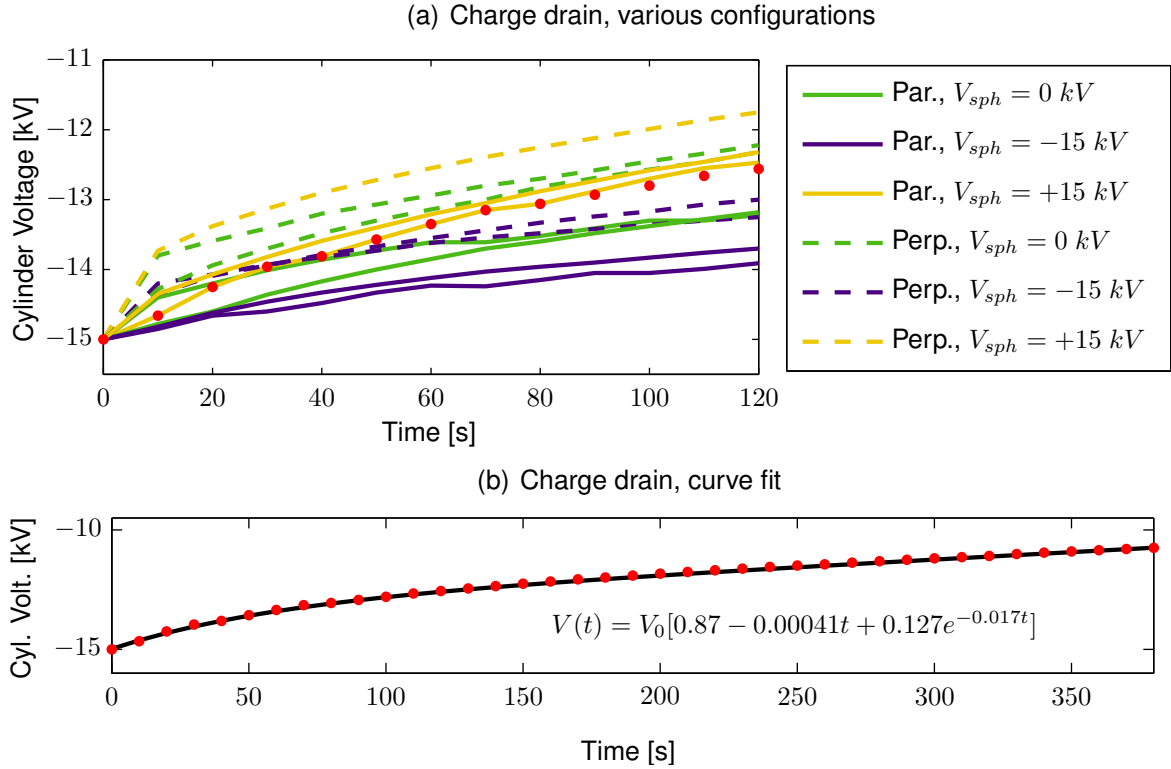

(a) Charge drain, various configurations

(b) Charge drain, curve fit

$$V(t) = V_0[0.87 - 0.00041t + 0.127e^{-0.017t}]$$

Figure 8. Characterization of charge drain on floating cylinder

It is important to remember that once the voltage lead has been removed and the charge has been delivered to the cylinder, changes in the orientation of the cylinder or the voltage level of the sphere will affect the electrostatic potential of the cylinder but not the total charge residing on its surface. To minimize the variation then, the charge should be deposited on the cylinder while the sphere is held grounded ($\phi_1 = 0$ V). The voltage measured on the cylinder by the surface voltmeter as the sphere potential switches polarity agrees with expected levels from the MSM, and switching does not affect the rate of charge drain. Moreover, voltage drain rates were measured at both smaller and positive initial voltages, and the remaining voltage scales linearly

with initial voltage, which allows for extrapolation to higher voltages. The total charge on the cylinder is also found to scale linearly with its voltage for a given orientation and sphere potential. Therefore, the sum of the charges q_2 sees a time-dependent reduction by $q_2(t) = q_{2,0}[0.87 - 0.00041t + 0.127e^{-0.017t}]$, which is the formulation used in the following simulations.

5 Active Charging Results

With the disturbance torques and passive charge drain on the cylinder fully character-ized, various simple charge control experiments are executed. The results are rigor-ously compared to an inclusive numerical simulation of the same system. MATLAB's 'ode45' function is used for the integration, while the three-sphere MSM is implemented to predict the Coulomb torques present on the rotating cylinder. First, active spin-up control is analyzed to determine at what angular velocity the drag and friction torques will balance the Coulomb torques from active charge control on the external sphere. Next, a de-spin control algorithm is implemented and compared to the natural velocity reduction resulting from bearing friction and atmospheric drag alone.

5.1 Spin-up Control

The voltage control algorithm outlined in Table 2 is applied to the sphere so that a con-stant rotation rate is maintained on the cylinder. When the angle falls within the dead band value θ_{DB} = 5 deg of the perpendicular and parallel cylinder configurations, zero potential is applied to the sphere. This ensures that uncertainties in the knowledge of the cylinder angle don't result in undesired torques on the cylinder. The simula-tion starts with a cylinder rate of ω_0 = 60 deg/s. Figure 9 displays various aspects of the experimental and simulated operation. As seen by the cylinder angular velocity in Figure 9(a), there is a very impressive level of agreement between the experimental and simulated results. While the oscillations in the experimental signal are likely due to measurement noise, the simulated rotation rate also shows some periodicity due to the complex Coulomb interactions. There even appears to be a slight oscillation in magnitude with a period of about 40 seconds that is evident in both curves, although there is no clear justification for this trend in the numerical simulation.

Table 2. Voltage control law for spin-up procedure

	$0° + \theta_{DB} < \theta < 90° - \theta_{DB}$ $180° + \theta_{DB} < \theta < 270° - \theta_{DB}$	$90° + \theta_{DB} < \theta < 180° - \theta_{DB}$ $270° + \theta_{DB} < \theta < 360° - \theta_{DB}$
CCW ($\omega > 0$)	ϕ_1 = -30 kV	ϕ_1 = +30 kV
CW ($\omega < 0$)	ϕ_1 = +30 kV	ϕ_1 = -30 kV

The voltage signals in Figure 9(b) exhibit the effect of the 0.8 second lag in the power supply as it switches polarity. When this lag is removed from the simulation, rotation rates up to 90 deg/s can be maintained. The voltage ϕ_2 on the cylinder varies slightly along with the switching polarity of the sphere voltage. Its slowly decreasing trend due to the charge drain is also visible. Figure 9(c) shows that the Coulomb torques achievable in this terrestrial system are about 4 times higher than the disturbances, which are dominated by atmospheric drag since the cylinder rotates above 50 deg/s. The Coulomb torques are not symmetric, because the induced charge effect causes

much higher torques in the opposite polarity attraction scenario than for the same polarity repulsion case.
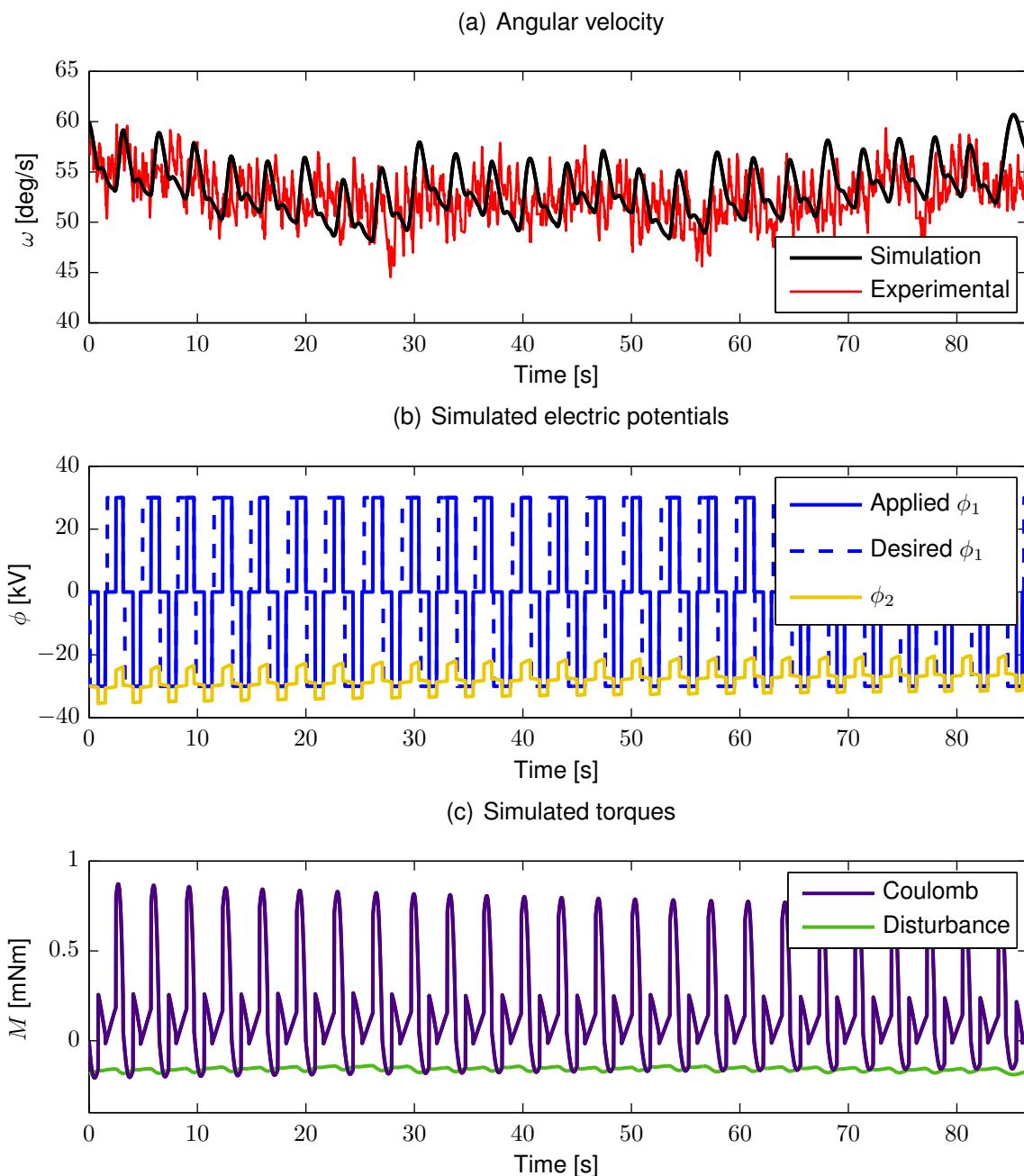
(a) Angular velocity

(b) Simulated electric potentials

(c) Simulated torques

Figure 9. Cylinder spin-up: experimental and simulation

5.2 De-spin Control

For the cylinder de-spin experiment, the exact opposite voltage control of Table 2 is applied to the sphere. Differentiation of the orientation signal is performed by the controller, using an in-situ version of the low-pass filter discussed in Section 3. A velocity dead band ω_{DB} = 4 deg/s is also applied to ensure that uncertainties in the differentiated velocity don't result in undesired torques as the cylinder comes to a halt. Figures 10(a) and 10(b) show the cylinder angle and rotation rate from both the physical experiment and the numerical simulation, with initial conditions θ_0 = 265 deg and

ω_0 = 105 deg/s. The majority of the rotation is removed from the system within 18 seconds, which is far shorter than the 50 seconds it takes to arrest the same rotation rate without Coulomb control as in Figure 8(a). This constitutes a successful demonstration of the Coulomb de-spin concept in a terrestrial environment. Without the delay in the power supply present, de-spin time is reduced to 14 seconds, which is a smaller difference than for the spin-up case. This is because the atmospheric drag torque is dominant at the higher rates, while the lag in the power supply is less severe for lower rates as the cylinder switches quadrants less rapidly. Plots of the applied voltages and moments are omitted for brevity.
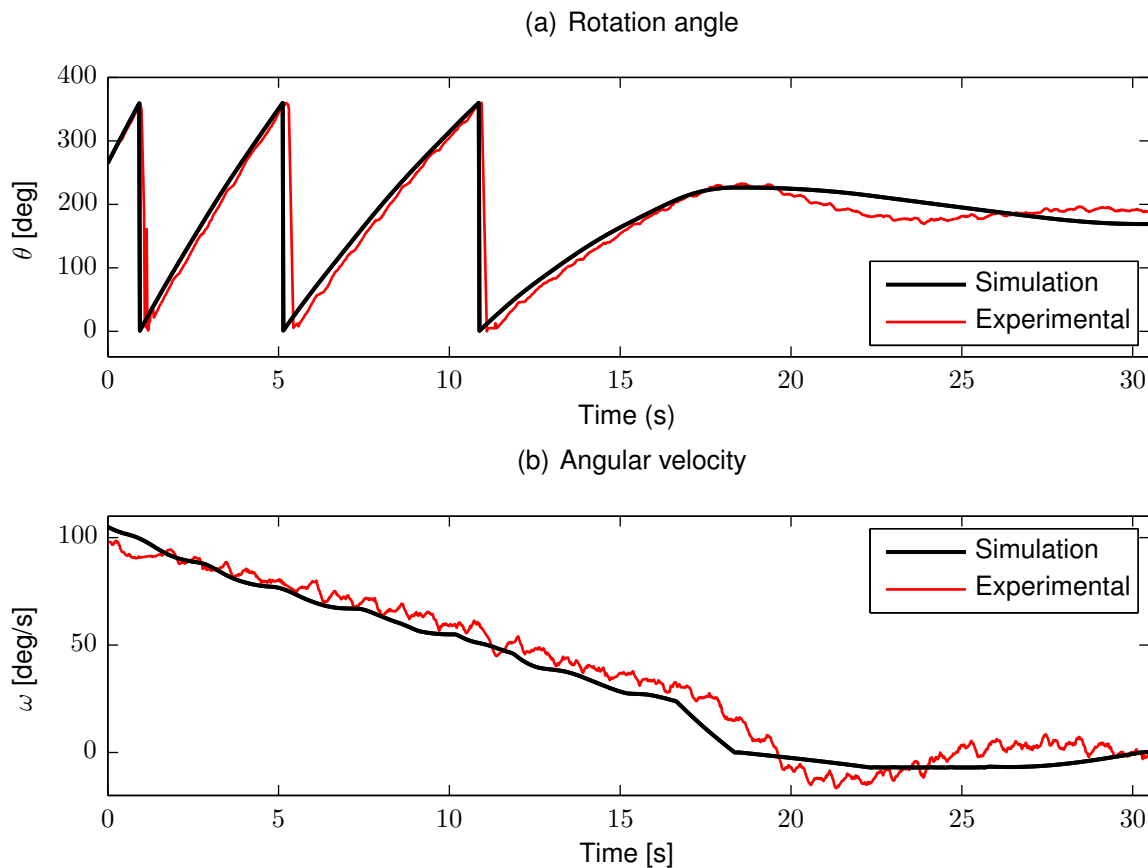
(a) Rotation angle

(b) Angular velocity

Figure 10. Cylinder de-spin: experimental and simulation

6   Conclusion

A terrestrial testbed has been created to verify the concept of remote attitude control by Coulomb charging. Various physical parameters in the system are characterized such as the charge drain from the floating potential cylinder and coefficients for the bearing friction and atmospheric drag. The disturbance torque from atmospheric drag is dominant at rotational speeds above 38 deg/s, below which the constant friction torque from the ceramic bearing dominates. Charge drain from the cylinder due to interaction with the atmosphere and its mount is minimal, as it retains 80% of its charge even after 3 minutes. Simulations using a Multi-Sphere Model with three spheres match exceptionally well with the experimental data, for both a charge controlled spin-up procedure and an active charged de-spin. Coulomb torques up to 4 times larger than the notable disturbance torques are achieved, and the largest impedance to the Coulomb

actuation is the delay present in the high voltage power supply when switching polarities. The noise and inaccuracies present in the current attitude encoding method are manageable for this application by signal processing, but in order to validate more precise attitude control algorithms, a more accurate means of encoding is desirable. In the end, this testbed represents a successful starting point for experimentally verifying charged spacecraft remote attitude control concepts.

Acknowledgments

References

[1] Olsen, R., "Experiments in charge control at geosynchronous orbit- ATS-5 and ATS-6," *Journal of Spacecraft and Rockets*, Vol. 22, No. 3, 1985, pp. 254–264.

[2] Mullen, E. G., Gussenhoven, M. S., Hardy, D. A., Aggson, T. A., Ledley, B. G., and Whipple, E., "SCATHA survey of high-level spacecraft charging in sunlight," *Journal of Geophysical Research: Space Physics*, Vol. 91, No. A2, 1986, pp. 1474–1490.

[3] King, L. B., Parker, G. G., Deshmukh, S., and Chong, J.-H., "Spacecraft Formation-Flying using Inter-Vehicle Coulomb Forces," Tech. rep., NASA/NIAC, January 2002.

[4] Schaub, H., Parker, G. G., and King, L. B., "Challenges and Prospect of Coulomb Formations," *Journal of the Astronautical Sciences*, Vol. 52, No. 1–2, Jan.–June 2004, pp. 169–193.

[5] Schaub, H. and Sternovský, Z., "Active Space Debris Charging for Contactless Electrostatic Disposal Maneuvers," *6th European Conference on Space Debris*, ESOC, Darmstadt, Germany, April 22–25 2013, Paper No. 6b.O-5.

[6] Jasper, L. E. Z. and Schaub, H., "Effective Sphere Modeling for Electrostatic Forces on a Three-Dimensional Spacecraft Shape," *AAS/AIAA Spaceflight Mechanics Meeting*, Girdwood, Alaska, July 31 – August 4 2011, Paper AAS 11–465.

[7] Rembala, R., Teti, F., and Couzin, P., "Operations Concept for the Robotic Capture of Large Orbital Debris," *35th Annual AAS Guidance & Control Conference*, AAS, Breckenridge, Colorado, February 3–8 2012, Paper No. AAS 12-018.

[8] Anderson, P. V. and Schaub, H., "Local Debris Congestion in the Geosynchronous Environment With Population Augmentation," *6th European Conference on Space Debris*, ESOC, Darmstadt, Germany, April 22–25 2013, Paper No. 3a.P-3.

[9] Schaub, H. and Moorer, D. F., "Geosynchronous Large Debris Reorbiter: Challenges and Prospects," *AAS Kyle T. Alfriend Astrodynamics Symposium*, Monterey, CA, May 17–19 2010, Paper No. AAS 10-311.

[10] Hogan, E. and Schaub, H., "Relative Motion Control for Two-Spacecraft Electrostatic Orbit Corrections," *AIAA Journal of Guidance, Control, and Dynamics*, Vol. 36, No. 1, Jan. – Feb. 2013, pp. 240–249.

[11] Wang, S., "Shape control of charged spacecraft cluster with two or three nodes," 2010.

[12] Seubert, C. R. and Schaub, H., "Electrostatic Force Model for Terrestrial Experiments on the Coulomb Testbed," *61st International Astronautical Congress*, International Astronautical Federation, Prague, CZ, Sept. 2010, Paper IAC-10.C1.1.9.

[13] Stevenson, D. and Schaub, H., "Multi-Sphere Method for Modeling Spacecraft Electrostatic Forces and Torques," *Advances in Space Research*, 2012.

[14] Stevenson, D. and Schaub, H., "Optimization of Sphere Population for Electrostatic Multi Sphere Model," *12th Spacecraft Charging Technology Conference, Kitakyushu, Japan*, 2012.

[15] Schaub, H. and Stevenson, D., "Prospects Of Relative Attitude Control Using Coulomb Actuation," *Jer-Nan Juang Astrodynamics Symposium*, College Station, TX, June 25–26 2012, Paper AAS 12–607.

[16] Smythe, W. R., *Static and Dynamic Electricity*, McGraw–Hill, 3rd ed., 1968.

[17] Sliško, J. and Brito-Orta, R. A., "On approximate formulas for the electrostatic force between two conducting spheres," *American Journal of Physics*, Vol. 66, No. 4, 1998, pp. 352–355.

[18] Seubert, C., "One-Dimensional Spacecraft Formation Flight Testbed for Terrestrial Charged Relative Motion Experiments," 2011.

[19] Tritton, D., *Physical Fluid Dynamics*, Oxford Science Publications, Clarendon Press, 1988.